

Membrane disruption of *Fusarium oxysporum* f. sp. *niveum* induced by myriocin from *Bacillus amyloliquefaciens* LZN01

Hengxu Wang,^{1,2,3} Zhigang Wang,^{1,2,3} Zeping Liu,^{1,3} Kexin Wang^{1,3} and Weihui Xu^{1,2,3*} 

¹College of Life Science and Agroforestry, Qiqihar University, Qiqihar 161006, China.

²Key Laboratory of Urban Agriculture, Ministry of Agriculture and Rural Affairs, Shanghai 200240, China.

³Heilongjiang Provincial Technology Innovation Center of Agromicrobial Preparation Industrialization, Qiqihar 161006, China.

Summary

Myriocin, which is produced by *Bacillus amyloliquefaciens* LZN01, can inhibit the growth of *Fusarium oxysporum* f. sp. *niveum* (Fon). In the present study, the antifungal mechanism of myriocin against Fon was investigated with a focus on the effects of myriocin on the cell membrane. Myriocin decreased the membrane fluidity and destroyed the membrane integrity of Fon. Significant microscopic morphological changes, including conidial shrinkage, the appearance of larger vacuoles and inhomogeneity of electron density, were observed in myriocin-treated cells. A membrane-targeted mechanism of action was also supported by transcriptomic and proteomic analyses; a total of 560 common differentially expressed genes (DEGs) and 285 common differentially expressed proteins (DEPs) were identified. The DEGs were further verified by using RT-qPCR. The combined analysis between the transcriptome and proteome revealed that the expression of some

membrane-related genes and proteins, mainly those related to sphingolipid metabolism, glycerophospholipid metabolism, steroid biosynthesis, ABC transporters and protein processing in the endoplasmic reticulum, was disordered. Myriocin affected the serine palmitoyl transferase (SPT) activity as evidenced through molecular docking. Our results indicate that myriocin has significant antifungal activity owing to its ability to induce membrane damage in Fon.

Introduction

Watermelon (*Citrullus lanatus*) is one of the most widely distributed fruit crops in the world (Dou *et al.*, 2018). However, the production of watermelon is seriously threatened by *Fusarium* wilt. *Fusarium oxysporum* f. sp. *niveum* (Fon), the causal agent of *Fusarium* wilt in watermelon, can survive for long periods and accumulate in soil. The symptoms of *Fusarium* wilt involve necrotic lesions, foliar wilting during pathogen invasion of the vascular system of watermelon plants, immature fruit and plant death (Costa *et al.*, 2018). The control of *Fusarium* wilt has been a challenge to watermelon producers as it is a devastating soilborne disease. Therefore, producers have opted to use chemical fungicides (Everts *et al.*, 2014); however, this is not an environment-friendly strategy.

Biological control is one of the most potential methods for soilborne disease owing to its advantages of environmental friendliness, safety and sustainability (Jiang *et al.*, 2015). Some bacterial strains have been evaluated as efficient biocontrol agents (BCAs) for suppressing soilborne disease; for example, *Bacillus amyloliquefaciens* SN16-1 has a high potential of controlling *F. oxysporum* f. sp. *lycopersici* (Wan *et al.*, 2018). *B. amyloliquefaciens* L3 can control Fon by producing diffusible and volatile organic compounds (Wu *et al.*, 2019). *B. velezensis* F21 can induce systemic resistance to Fon in watermelon through related genes and phytohormone signalling factors (Jiang *et al.*, 2019).

Studies on the biocontrol mechanisms of BCAs have progressed in recent years. The biocontrol mechanisms operating against pathogens involve changes in soil microbial diversity, inducing systemic resistance and the production of diffusible and volatile antimicrobial compounds. The biocontrol activity of BCAs is related to the

Received 13 April, 2020; revised 10 August, 2020; accepted 14 August, 2020.

*For correspondence. E-mail xwh800206@163.com; Tel. +86 0452 2738781; Fax +86 0452 2738781.

Microbial Biotechnology (2021) 14(2), 517–534
doi:10.1111/1751-7915.13659

Funding information

The authors gratefully acknowledge the funding of this work by the National Natural Science Foundation of China (31700428), the Joint Guiding Project of Natural Science Foundation in Heilongjiang Province, China (LH2019C068), the Open Foundation of Key Laboratory of Urban Agriculture, the Ministry of Agriculture and Rural Areas, China (UA201904), and the Scientific Research Program at Qiqihar University, China (135209266).

[Correction added on 01 October 2020 after first online publication: The affiliations for authors Hengxu Wang and Weihui Xu have been updated in this version.]

© 2020 The Authors. *Microbial Biotechnology* published by Society for Applied Microbiology and John Wiley & Sons Ltd

This is an open access article under the terms of the Creative Commons Attribution-NonCommercial-NoDerivs License, which permits use and distribution in any medium, provided the original work is properly cited, the use is non-commercial and no modifications or adaptations are made.

production of antibiotic compounds including lipopeptides (LPs) (Koumoutsis *et al.*, 2004; Molinatto *et al.*, 2016). These LPs are of the iturin (such as bacillomycin D/F/L/Lc, iturin A/C and mycosubtilin), fengycin (fengycin A/B and plipastatin A/B) and surfactin (halobacillin, pumilacidin and surfactin) classes; these are major contributors to *Bacillus* biocontrol activity. For instance, *B. amyloliquefaciens* FZB42 produces fengycin and bacillomycin D, which show synergistic antagonistic activity against *Fusarium oxysporum* (Koumoutsis *et al.*, 2004). Fengycin and surfactin of the *B. subtilis* strain SG6 have been considered to contribute to the inhibition of *F. graminearum* growth (Zhao *et al.*, 2014). Surfactin, iturin and fengycin produced by *B. velezensis* Y6 and Y7 were reported to be responsible for the antimicrobial activity against *Ralstonia solanacearum* and *Fusarium oxysporum* (Cao *et al.*, 2018). Bacillomycin D, which is secreted by *B. velezensis* SQR9, can bind to the iron transport regulator Btr and modulate biofilm formation through the KinB-Spo0a-SinI-SinR pathway to suppress the growth of *Fusarium oxysporum* (Xu *et al.*, 2013). Phenazine-1-carboxamide, which is secreted by *Pseudomonas piscium*, can affect the activity of the fungal protein FgGcn5 that would thereby lead to the deregulation of histone acetylation at H2BK11, H3K14, H3K18 and H3K27 in *Fusarium graminearum* and eventually cause fungal death (Chen *et al.*, 2018). The plasma membrane is the primary target of some LPs and antimicrobial compounds (Li *et al.*, 2015). In a study, iturin has been reported to negatively affect the cytoplasmic membranes of yeast cells wherein the leakage of K⁺ ions and the growth of cell were affected (Ongena and Jacques, 2008). Fengycin also has been reported to cause perturbation, bending and pore formation on artificial membranes (Patel *et al.*, 2011; Falardeau *et al.*, 2013). Antimicrobial substances directly act on the cell membrane of pathogens, enhance membrane permeability and cause cell death (Li *et al.*, 2015). The electrostatic interactions between chensinin-1b and lipopolysaccharide can facilitate the disruption of the cytoplasmic membranes of *Escherichia coli* and *Staphylococcus aureus* (Sun *et al.*, 2015).

Myriocin, a sphingosine analogue with antifungal antibiotic properties (De Melo *et al.*, 2013), reduces the synthesis of sphingolipid compounds by inhibiting the activity of serine palmitoyl transferase (SPT) (Wadsworth *et al.*, 2013). Sphingolipids are plasma membrane lipid constituents in eukaryotic cells (Yamaji-Hasegawa *et al.*, 2005). In a previous study, we found that sphingofungin compounds are secreted by *B. amyloliquefaciens* LZN01; myriocin was one of the secreted sphingofungin compounds that inhibited the growth of *Fon*, and its minimum inhibitory concentration (MIC) was 1.25 µg ml⁻¹ (Xu *et al.*, 2019). However, there is limited information about the effect of myriocin on the cell membrane of *Fon*.

Omics technologies provide powerful tools for characterizing the modes of action of antimicrobial compounds in pathogens (Massart *et al.*, 2015). However, the study of the mechanisms of action of myriocin on the cell membrane of *Fon* through proteomic and transcriptomic analyses has not yet been reported. In this study, we aimed (i) to evaluate the effect of myriocin on the microscopic morphology of conidia and membrane integrity and fluidity of *Fon*, (ii) to examine membrane perturbation by measuring calcein leakage from calcein-loaded liposomes, (iii) to reveal the effect of myriocin on the gene expression at the mRNA and protein levels that would subsequently provide insights into the mechanism of myriocin action on the cell membrane of *Fon* and (iv) to analyse the enzyme activity of SPT and characterize the mode of myriocin action on SPT by simulating molecular docking. This study aimed to understand the damage mechanisms of myriocin on the cell membrane of *Fon* and to lay a good foundation for the application of *B. amyloliquefaciens* LZN01 in the future.

Results

Effect of myriocin on the microscopic morphology of Fon conidia

The morphological changes observed in *Fon* conidia that were exposed to myriocin for 12 h are shown in Figure 1. SEM imaging showed that *Fon* conidia were replete and had smooth surfaces in the negative control (CK1). In contrast, the *Fon* conidia treated with myriocin (MIC-8MIC, 1.25 µg ml⁻¹–10 µg ml⁻¹) and amphotericin B (CK2) exhibited morphological abnormalities including surface indentation and shrinkage deformation; the indentation on the conidial surface deepened as the concentration of myriocin was increased (Fig. 1A). TEM micrographs of *Fon* conidia in the negative control (CK1) showed that the cell nucleus and a small number of vacuoles were visible and that the electron density in the cytoplasm was homogeneous. In contrast, the *Fon* conidia treated with amphotericin B (CK2) and myriocin exhibited abnormalities, including the appearance of larger vacuoles (blue arrows), separation of the cell wall and cytoplasm (red arrows), and inhomogeneity of electron density in the cytoplasm (Fig. 1B). This result indicated that myriocin damaged the morphology and affected the internal structure of the conidia; these effects contributed to the growth inhibition of *Fon*.

Effect of myriocin on Fon cell membrane integrity

SYTO 9 and propidium iodide (PI) dye, which can distinguish the intact from membrane-damaged cells, were used to analyse the membrane integrity of *Fon*. SYTO 9 generally stains live and dead cells in a population,

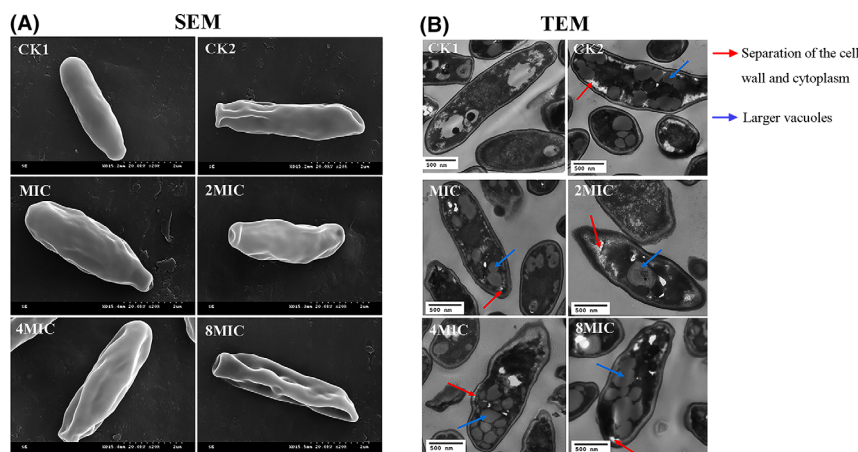


Fig. 1. SEM (A) and TEM (B) images of *Fon* conidia exposed to amphotericin B and various myriocin concentrations. CK1, 0 $\mu\text{g ml}^{-1}$ myriocin; MIC, 1.25 $\mu\text{g ml}^{-1}$ myriocin; 2MIC, 2.5 $\mu\text{g ml}^{-1}$ myriocin; 4MIC, 5 $\mu\text{g ml}^{-1}$ myriocin; 8MIC, 10 $\mu\text{g ml}^{-1}$ myriocin; CK2, 1.25 $\mu\text{g ml}^{-1}$ amphotericin B.

whereas PI penetrates cells with damaged membranes and causes a reduction in SYTO 9 fluorescence when both dyes are present. Thus, the cells with intact membranes emit green fluorescence, whereas the cells with damaged membrane emit red fluorescence. The *Fon* conidia in the negative control (CK1) emitted green fluorescence under confocal laser scanning microscopy (CLSM); this indicated that the cell membranes were intact. After 12 h amphotericin B (CK2), a small amount of green fluorescence was observed; this may be related to the reduction in membrane integrity. After culturing with different concentrations of myriocin for 12 h, the intensity of red fluorescence increased as the concentration of myriocin was increased (Fig. 2). In myriocin-treated cells (MIC–8MIC, 1.25 $\mu\text{g ml}^{-1}$ –10 $\mu\text{g ml}^{-1}$), the dead cells (red fluorescence) increased from 54.9% to 77.3%, and the hypoactive cells (yellow fluorescence) decreased from 26.5% to 9.1% (Fig. S1). This suggests that myriocin damaged the cell membranes of *Fon*, which thereby resulted in a large number of cell deaths.

Membrane fluidity and calcein leakage

The 1,6-diphenyl-1,3,5-hexatriene (DPH) fluorescence polarization is closely related to the fluidity of the cell membrane; in other words, the increase in membrane fluidity implies that the fluorescence polarization (P) and anisotropy (r) will decrease (Cavanagh *et al.*, 2019). Compared with CK1, the P and r of the *Fon* conidia exposed to different concentrations of myriocin significantly increased (Fig. 3A). The increase in P and r indicated that exposure to myriocin decreased the membrane fluidity of *Fon*. However, no significant difference in the P and r of the *Fon* conidia among MIC, 2MIC and 4MIC treatments was found. Maybe, the

conidia survived in similar way after 12-h exposure to those myriocin treatments.

To determine whether the *Fon* cell membrane can be preferentially targeted by myriocin, membrane perturbation was examined by measuring the calcein leakage from phosphatidylcholine (PC)/phosphatidylethanolamine (PE)/phosphatidylinositol (PI)/ergosterol (5:4:1:2, w/w/w/w) liposomes. As shown in Figure 3B, encapsulated calcein was rapidly leaked from the liposomes upon exposure to different concentrations of myriocin. MIC (1.25 $\mu\text{g ml}^{-1}$), 2MIC (2.50 $\mu\text{g ml}^{-1}$), 4MIC (5.0 $\mu\text{g ml}^{-1}$) and 8MIC (10 $\mu\text{g ml}^{-1}$) of myriocin induced 41.7%, 54.5%, 63.4% and 68.3% leakage from the liposomes in 12 min, respectively. However, the calcein leakage from the liposomes in the control (CK1) was only 3.7%. These results demonstrated that myriocin caused damage to the membrane and that calcein escaped the liposomes through myriocin-induced pores. Upon the addition of 10% Triton X-100 at 12 min, an additional 20–76% increase in calcein leakage from liposomes was observed, and complete leakage of calcein (100%) was detected at 18 min.

GO functional annotation, KEGG pathway enrichment and expression analysis of DEGs and DEPs

In the present study, membrane-related DEGs and DEPs were investigated by using combined transcriptome and proteome analyses. At the protein level, a total of 651 DEPs were identified by using a statistical criterion (fold changes ≥ 1.2 or ≤ 0.83 , P -value < 0.05). Among them, 584 and 352 DEPs belonged to CK1_VS_MIC and CK1_VS_8MIC, respectively; 285 common DEPs in both CK1_VS_MIC and CK1_VS_8MIC (Fig. 4A) were found. Of the 285 common DEPs, 135 and 150 proteins were

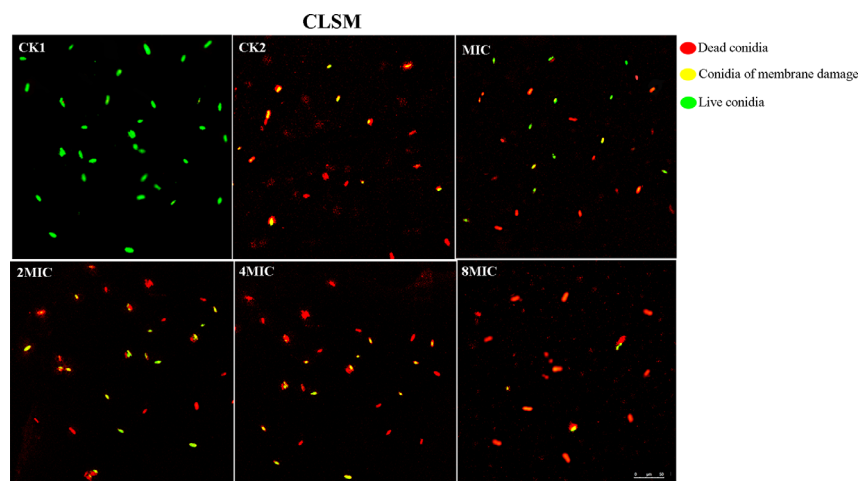


Fig. 2. Effect of myriocin on *Fon* cell membrane integrity. CK1, $0 \mu\text{g ml}^{-1}$ myriocin; MIC, $1.25 \mu\text{g ml}^{-1}$ myriocin; 2MIC, $2.5 \mu\text{g ml}^{-1}$ myriocin; 4MIC, $5 \mu\text{g ml}^{-1}$ myriocin; 8MIC, $10 \mu\text{g ml}^{-1}$ myriocin; CK2, $1.25 \mu\text{g ml}^{-1}$ amphotericin B.

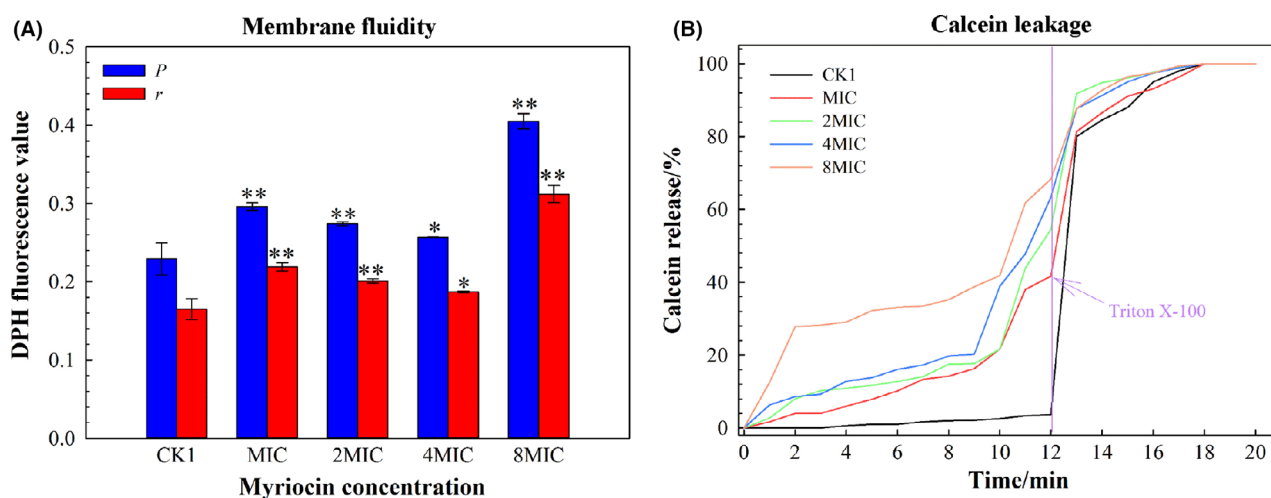


Fig. 3. Influences of myriocin on the membrane fluidity of *Fon* (A) and time courses for the leakage of calcein (B) after the addition of myriocin. CK1, $0 \mu\text{g ml}^{-1}$ myriocin; MIC, $1.25 \mu\text{g ml}^{-1}$ myriocin; 2MIC, $2.5 \mu\text{g ml}^{-1}$ myriocin; 4MIC, $5 \mu\text{g ml}^{-1}$ myriocin; 8MIC, $10 \mu\text{g ml}^{-1}$ myriocin. The arrow indicates the addition of 10% Triton X-100 at 12 min. Significant differences between treatment and control (CK1) are indicated by '*' ($*P \leq 0.05$ and $**P \leq 0.01$, independent samples *t*-test).

significantly downregulated and upregulated under myriocin exposure respectively (Fig. 4B).

At the mRNA level, 1161 DEGs were identified (fold changes ≥ 2 or ≤ 0.5 , P -value ≤ 0.05). There were 560 common DEGs in both CK1_VS_MIC and CK1_VS_8MIC (Fig. 4A), of which 226 genes were significantly upregulated and 334 genes were significantly downregulated under myriocin exposure (Fig. 4B).

The common DEPs and DEGs were classified by using GO functional annotation. The DEPs and DEGs were mainly enriched in cellular components, such as membrane part, membrane, cell and cell part. Among them, the DEPs were mainly involved in the cell (66.6%) and cell part (66%), and the DEGs were involved in the

membrane (93.6%) and membrane part (88.9%) (Fig. 4C). As shown in Figure 4C, a large percentage of DEPs and DEGs were involved in the membrane and membrane parts.

KEGG pathway enrichment analysis was performed. As shown in Figure 5A, all the common DEPs and DEGs were combined and significantly enriched in the top five pathways: ABC transporters, steroid biosynthesis, sphingolipid metabolism, glycerophospholipid metabolism and protein processing in the endoplasmic reticulum. A total of 27 DEPs (Table S2) and 26 DEGs (Table S3) were enriched in these five pathways. Protein processing in the endoplasmic reticulum was the most enriched pathway in the proteome analysis, and steroid

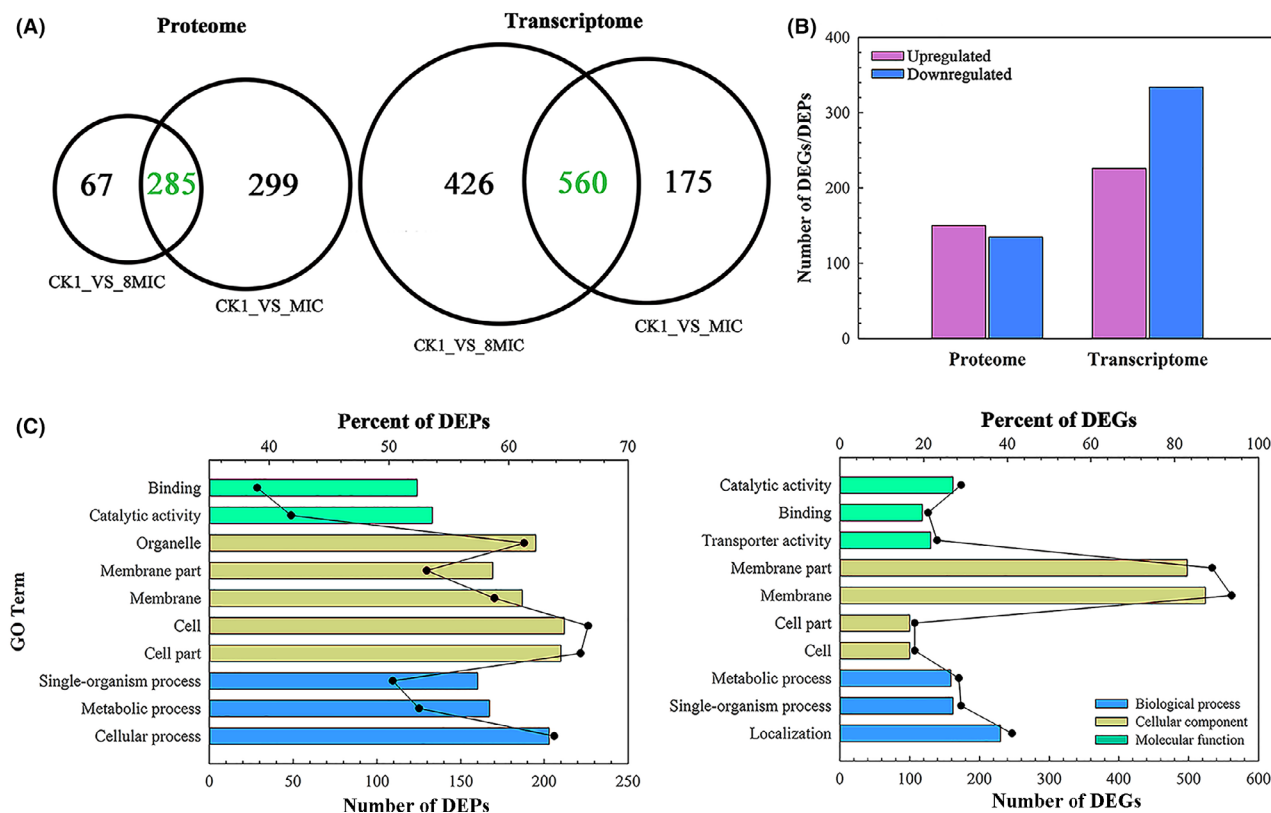


Fig. 4. Venn diagram, number and GO functional annotations of the DEGs and DEPs ($P < 0.05$). CK1, $0 \mu\text{g ml}^{-1}$ myriocin; MIC, $1.25 \mu\text{g ml}^{-1}$ myriocin; 8MIC, $10 \mu\text{g ml}^{-1}$ myriocin.

A. Venn diagram of the DEGs and DEPs in CK1_VS_MIC and CK1_VS_8MIC. This figure was performed by using Funrich 3.0.

B. The number of common DEGs or DEPs in both CK1_VS_MIC and CK1_VS_8MIC.

C: GO functional annotation of DEPs and DEGs. GO categories significantly enriched ($P < 0.05$) are shown in the figure. The ordinate represents the GO term, the inner abscissa represents the number of DEPs or DEGs (column) and the upper abscissa represents the per cent (dot). The biological process, cellular component and molecular function are represented by blue, yellow and green, respectively.

biosynthesis was the most enriched pathway in the transcriptome analysis. In addition, three pathways (steroid biosynthesis, sphingolipid metabolism and glycerophospholipid metabolism) belonged to the lipid metabolism category; protein processing in the endoplasmic reticulum belonged to the folding, sorting and degradation category, and ABC transporters belonged to the membrane transport category (Table S4). The results indicated that some membrane-related genes and proteins were affected by myriocin and were involved in some metabolic pathways.

As shown in the clustering heatmap (Fig. 5B and Table 1), 14 DEGs and 13 DEPs were downregulated, and 12 DEGs and 14 DEPs were upregulated. The upregulated DEGs were mainly enriched in sphingolipid metabolism and steroid biosynthesis. The downregulated DEGs were mainly enriched in protein processing in the endoplasmic reticulum and glycerophospholipid metabolism. The upregulated DEPs were mainly enriched in glycerophospholipid metabolism, sphingolipid metabolism

and protein processing in the endoplasmic reticulum. The downregulated DEPs were enriched in glycerophospholipid metabolism and protein processing in the endoplasmic reticulum. In addition, the expression of genes and proteins was significantly changed in the ABC transporter pathway.

Correlation of expression levels and protein interaction network analysis

To further determine the target of membrane damage, a correlation analysis of DEG expression levels was performed by using the Spearman algorithm (correlation coefficients ≥ 0.5 , q -value = 0.05), and protein-protein interaction (PPI) network analysis was performed by using the STRING database (combined score ≥ 0.4).

The correlation of the expression levels of 26 DEGs was divided into three parts. The first part consisted of 7 DEGs in steroid biosynthesis, 3 DEGs in sphingolipid metabolism and 2 DEGs in ABC transporters. The

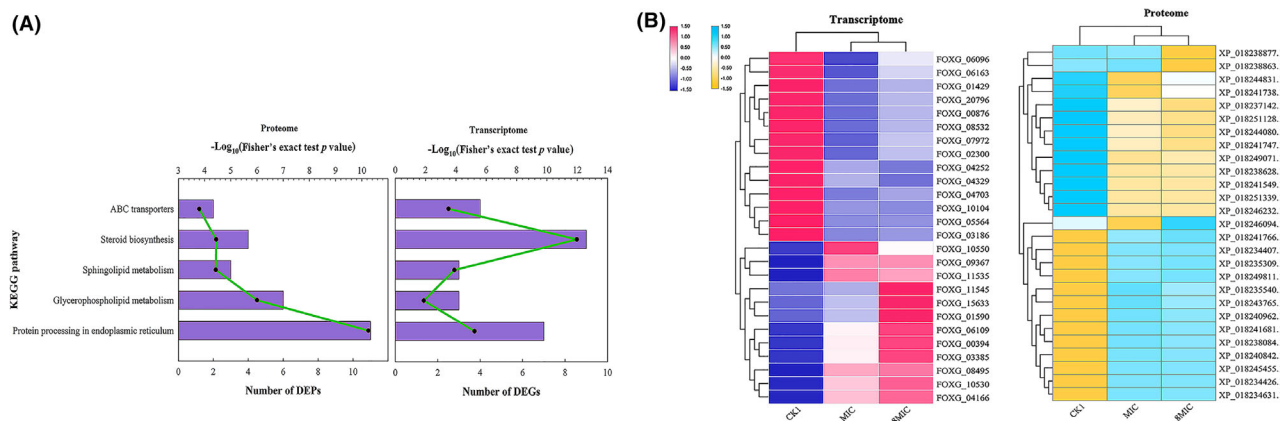


Fig. 5. KEGG pathway enrichment and clustering heatmaps of the DEGs and DEPs.

A. Significantly enriched KEGG pathways are shown in the figure. The ordinate represents the KEGG pathway names, the nether abscissa (column) represents the number of DEGs or DEPs, and the upper abscissa (dot) represents the significance level of enrichment.

B. Clustering heatmap of DEPs and DEGs. The colours indicate the expression level of the gene/protein [$\log_{10}(\text{TPM} + 1)$]. A tree diagram of gene/protein clustering is shown on the left. The gene names/protein NCBI accession numbers are shown on the right. The two genes/proteins belong to same branch, which indicates their expression levels are similar.

Table 1. The number of upregulated and downregulated DEGs (26) and DEPs (27) in five pathways.

Pathway ID	Pathway name	Number of DEGs		Number of DEPs	
		Up	Down	Up	Down
map00564	Glycerophospholipid metabolism	0	3	3	3
map00600	Sphingolipid metabolism	3	0	3	0
map00100	Steroid biosynthesis	7	2	2	2
map04141	Protein processing in endoplasmic reticulum	0	7	5	7
map02010	ABC transporters	2	2	1	1

Five pathways are glycerophospholipid metabolism pathway, sphingolipid metabolism pathway, steroid biosynthesis pathway, protein processing in endoplasmic reticulum pathway and ABC transporters pathway, respectively.

second part consisted of 2 DEGs in glycerophospholipid metabolism and 1 DEG in protein processing in the endoplasmic reticulum. The third part consisted of 2 DEGs in glycerophospholipid metabolism, 1 DEG in ABC transporters, 2 DEGs in steroid biosynthesis and 6 DEGs in protein processing in the endoplasmic reticulum. *FOXG_08532* in the third part was correlated with the expression levels of the 7 DEGs, and the correlation of *FOXG_08532* with other genes was the greatest among all DEGs (Fig. 6A). The results indicated that 26 DEGs from different pathways were correlated, and we speculate that myriocin affected the expression of *FOXG_08532* and triggered a series of reactions related to *FOXG_08532*.

In the PPI network, a total of 24 DEPs interacted. XP_018237142.1 (methylene-fatty-acyl-phospholipid

synthase) is involved in the glycerophospholipid metabolism pathway. The degree centrality, closeness centrality and betweenness centrality values of XP_018237142.1 were 0.3, 0.44 and 0.64 (Fig. 6C), respectively, and these values were higher for XP_018237142.1 than for the other proteins. The results showed that methylene-fatty-acyl-phospholipid synthase was the core protein, which thereby indicated that it plays an important role in interacting with the protein network (Fig. 6B). This methylene-fatty-acyl-phospholipid synthase interacted not only with 5 DEPs in the glycerophospholipid metabolism pathway but also with XP_018249071.1 (DnaJ-like subfamily B member 12) and XP_018240962.1 (hypothetical protein FOXG_05558) in protein processing in the endoplasmic reticulum pathway. In addition, the top six DEPs in Figure 6C are involved in the glycerophospholipid metabolism pathway, sphingolipid metabolism pathway and steroid biosynthesis pathway. The results showed that the expression levels of some proteins involved in the above metabolism pathway were affected by myriocin.

The relationship between the DEGs and DEPs was analysed by combining the transcriptome data, proteome data and PPI network. The interactions of proteins encoded by 25 DEGs were predicted, and a total of 6 candidates overlapped in the transcriptome and proteome data sets (Table S5). Six candidate DEPs belonged to the PPI network (Fig. 6B); *FOXG_01590*, *FOXG_03186*, *FOXG_11535*, encoding C-8 sterol isomerase (XP_018234407.1), methylene-fatty-acyl-phospholipid synthase (XP_018237142.1) and serine palmitoyl transferase (XP_018249811. 1) played an important role in the interaction of genes (Fig. 6D and

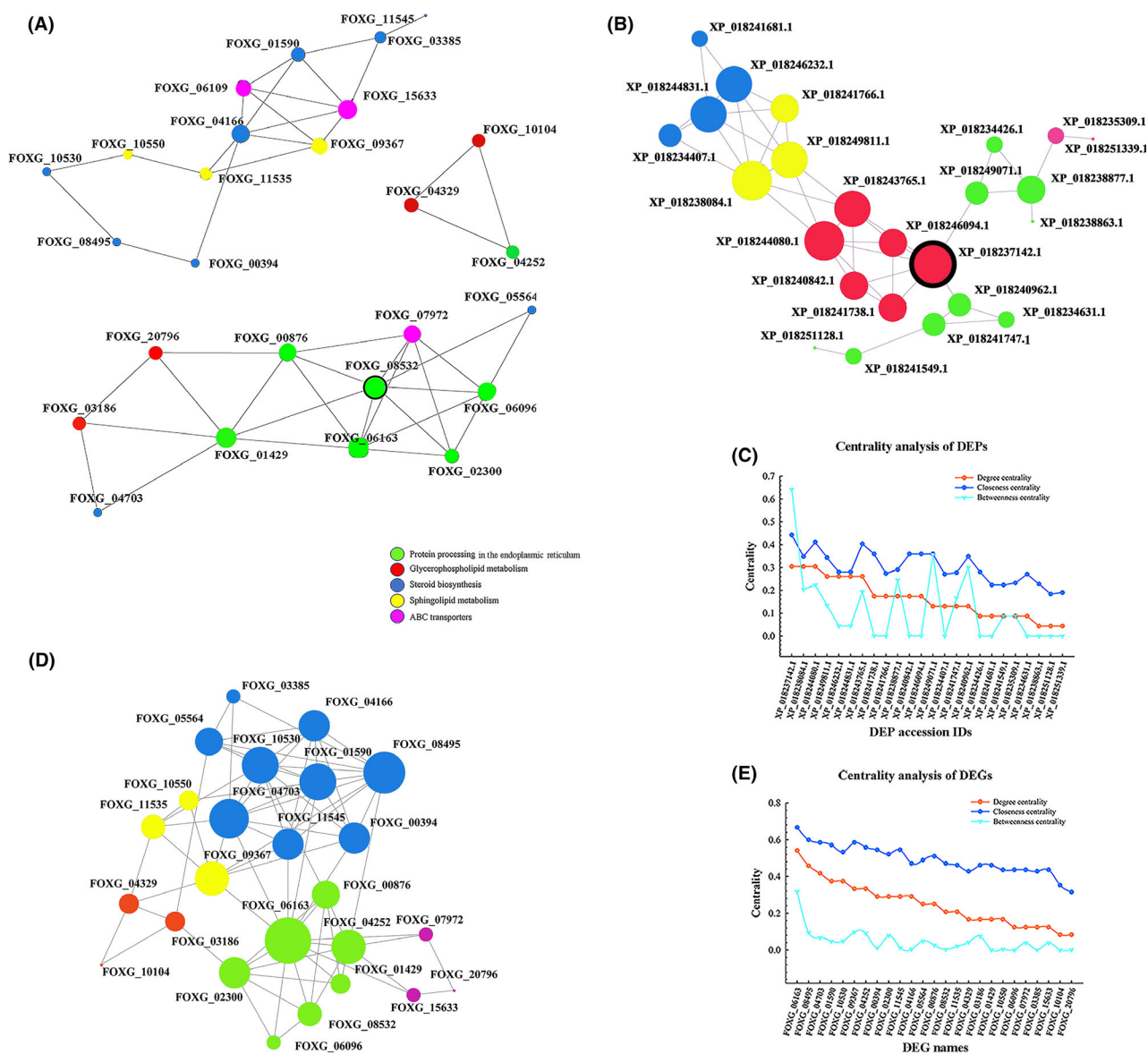


Fig. 6. Correlation analysis of expression levels among 26 DEPs, interaction networks of DEPs and distribution of network centre coefficient. (A) Each node represents a DEG, and a connection represents the correlation of DEGs. The size of the node represents correlations with the other DEGs. The colours of node represent five pathways. (B) Diagram of interaction network among DEPs. The nodes represent DEPs which are shown by NCBI accession ID. The size of a node is proportional to its connectivity (degree). The larger the node is, the more important it is in the network. (D) Prediction of DEGs-encoded proteins interaction networks. The nodes represent DEGs-encoded proteins, and the names of the nodes are displayed by gene name. (C and E) Distribution of the network centre coefficient. The abscissa represents the NCBI accession ID/gene name. The ordinate represents the centrality, including betweenness centrality, degree centrality and closeness centrality. The larger the three values are, the more important the node is in maintaining connection of entire network, the higher the centrality degree of the node is, and the closer the node is to the network centre.

E). The methylene-fatty-acyl-phospholipid synthase (XP_018237142.1) and serine palmitoyl transferase (XP_018249811.1) were 2 of the top six DEPs (Fig. 6C). The *FOXG_01590* and *FOXG_11535* correlated with the expression levels of other DEGs (Fig. 6A). The combined analysis of the transcriptomic and proteomic data indicated that myriocin might target *FOXG_01590* or *FOXG_11535*, change the expression

of the proteins and finally affect the function of the cell membrane.

RT-qPCR analysis

To confirm the RNA-Seq data, the expression of 9 typical genes was analysed by using RT-qPCR. The expression levels of *FOXG_04166* and *FOXG_11535* in

myriocin-treated cells were significantly increased with reference to those in the control; and the expression levels of *FOXG_07972*, *FOXG_03186*, *FOXG_01897*, *FOXG_07760*, *FOXG_04703*, *FOXG_02300*, *FOXG_04252*, *FOXG_06096* and *FOXG_01429* were significantly decreased in myriocin-treated cells (Fig. 7). The trend of expression of 9 genes was consistent with the transcriptome analysis results.

Assay of SPT activity and molecular docking with myriocin

To confirm the differential expression of SPT according to proteomics analysis, SPT activity was measured by using ELISA. As shown in Figure 8A, the SPT activities were higher in the MIC and 2MIC treatments than in the control (CK1). Interestingly, there was a significant decrease in SPT activity in 8MIC treatment compared with that in CK1. These suggest that the response of SPT activity to different concentrations of myriocin were different.

Molecular docking is a key tool in predicting the binding modes of ligand–protein interactions and is increasingly popular for studying ligand–protein interactions (Thomsen and Christensen, 2006). Based on proteomics analysis, the SPT (XP_018249811.1) encoded by *FOXG_11535* exhibited differential expression in myriocin-treated cells. To verify the interaction between myriocin and SPT, a molecular docking of myriocin to the 3D protein model of SPT (XP_018249811.1) was performed. Figure 8B shows the 3D conformation of myriocin with the best docking model and with a low grid score of $-60.5 \text{ kcal mol}^{-1}$. Shown in Figure 8C is a myriocin bound to the internal

active site of SPT. The fatty acid hydrocarbon chain of myriocin inserted into a hydrophobic pocket of SPT and formed a hydrophobic interaction. The polar portion of myriocin interacted with several amino acid residues located in the active site of SPT. Two hydroxyl groups (a and b) of myriocin and Asn325 formed hydrogen bonds. The hydroxyl group c of myriocin and Leu324 formed a hydrogen bond, and the hydroxyl group d of myriocin and Ala563 formed another hydrogen bond. The amidogens of myriocin and Ala563 and Pro562 also formed hydrogen bonds. Moreover, the carboxyl group of myriocin and Arg330 formed a hydrogen bond. Myriocin provided hydrogen, and the amino acid residues of SPT accepted hydrogen, leading to an interaction between myriocin and SPT. The results showed that myriocin and SPT formed hydrophobic interactions and seven hydrogen bonds; this might be what could have led to the stable interaction between myriocin and SPT, wherein the biological activity and function of SPT were inhibited.

Discussion

In the present study, we focused on understanding the mechanism of action of myriocin in *Fon*. SEM and TEM observations showed that the growth inhibition of *Fon* in response to myriocin was accompanied by conspicuous morphological and cytological changes, including shrivelled cell surface, condensation of the cytoplasm, appearance of larger vacuoles, and the separation of cell wall and cytoplasm. These effects were similar to those of some antibiotics (Yan *et al.*, 2010; Zhang *et al.*, 2013, 2016). In a study, the formation of larger vacuoles has

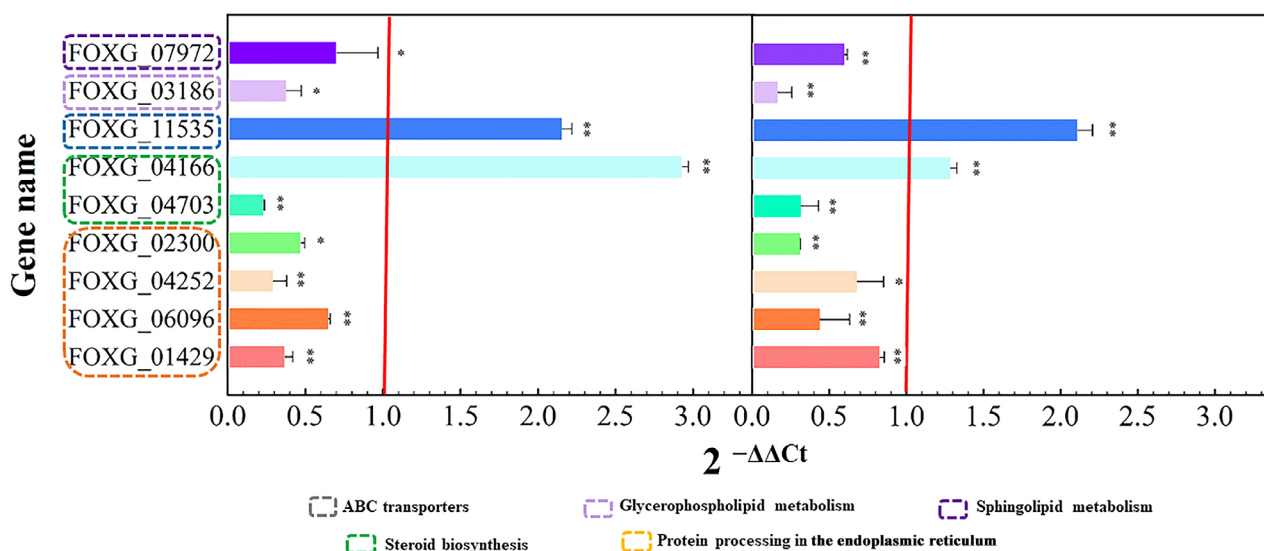


Fig. 7. Validation of RNA-seq data using RT-qPCR. The left panel represents the RNA-seq data, and the right panel represents the mean values of \log_2 (fold change) observed for the 8MIC myriocin treatment vs. CK1 ($*P \leq 0.05$, $**P \leq 0.01$). The different colours of the lined boxes represent different pathways.

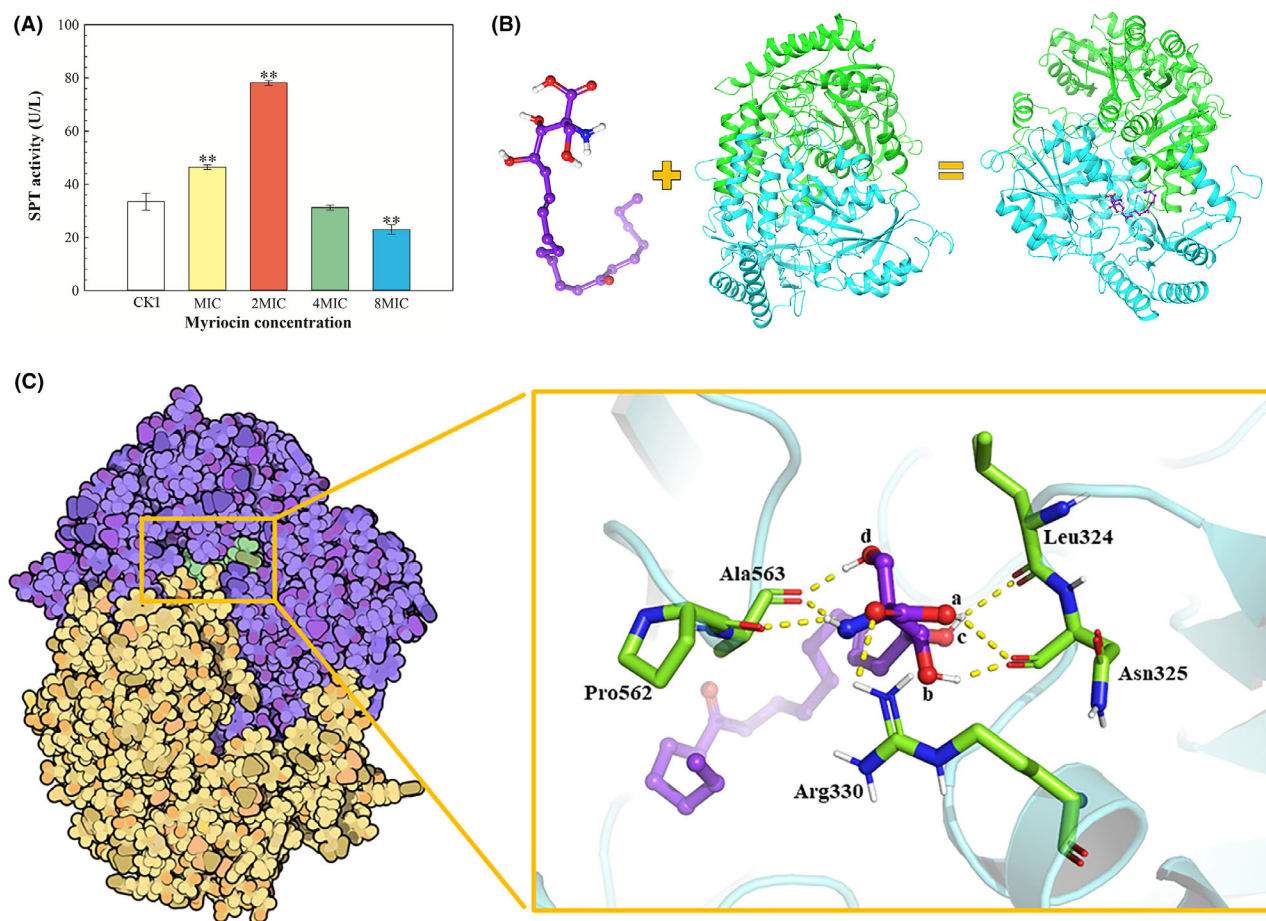


Fig. 8. SPT activity of *Fon* cells in myriocin-treated, 3D diagram, and surface drawing of molecular docking of myriocin to SPT. CK1, 0 $\mu\text{g ml}^{-1}$ myriocin; MIC, 1.25 $\mu\text{g ml}^{-1}$ myriocin; 2MIC, 2.5 $\mu\text{g ml}^{-1}$ myriocin; 4MIC, 5 $\mu\text{g ml}^{-1}$ myriocin; 8MIC, 10 $\mu\text{g ml}^{-1}$ myriocin.

A. SPT activity of *Fon*. Significant differences between treatment and control (CK1) are indicated by ** (** $P \leq 0.01$, independent samples t -test).

B. 3D structures of SPT and the best 3D conformation of myriocin. The protein is shown as ribbons with one subunit in green and the other subunit in blue. Myriocin is shown as a stick: C in purple, N in dark blue, O in red, H in white.

C. A detailed 3D diagram of molecular docking of myriocin to SPT. Surface drawing of myriocin-SPT binding is shown: one subunit is in purple, the other subunit is in yellow, and myriocin is in green (left). 3D diagram of myriocin bind to the internal active site of SPT (right). Myriocin and amino acid residues are shown as sticks. Carbon, nitrogen, oxygen and hydrogen atoms in amino acid residues are shown in green, blue, red, and white, respectively. Atoms in myriocin are coloured (see B legend for details). Hydroxyl groups of myriocin are indicated by different letters (a, b, c, and d). The distance between the two electronegative atoms in the hydrogen bond is 3 Å. Hydrogen bonds are shown as yellow dashed lines, and the residues in the binding site are labelled.

been reported to be closely related to antifungal activity (Thimon *et al.*, 1995).

Some studies have indicated that some antifungals target the plasma membrane (Spampinato and Leonard, 2013; Lee and Lee, 2015). The propidium iodide influx assay can reveal the loss of membrane integrity and pore formation in the cell membrane (Spir *et al.*, 1995). Hence, cells without a cell membrane or damaged cell membrane are considered dead cells (Gumbo *et al.*, 2014; Cronjé and Gaynor, 2019). In this study, we determined by using CLSM that the number of dead cells increased as the concentration of myriocin was increased (Fig. 2); this indicates that myriocin

damaged membrane integrity and caused cell death (Li *et al.*, 2012). A similar result was observed in the mimic membranes of liposomes. Myriocin can induce calcein leakage from PC/PE/PI/ergosterol liposomes (Fig. 3B), which thereby suggests that calcein escape from liposomes might be related to myriocin-induced pore formation. Damage to membrane integrity and shrinkage of cell occurs along with the loss of ions or intracellular components (Cho *et al.*, 2013). In this study, the shrinkage of myriocin-treated *Fon* conidia was observed by using SEM (Fig. 1A); this result might be related to myriocin inducing injury to the membrane.

Membrane fluidity affects membrane functions such as biochemical reactions, protein secretion, ion transport and permeability (Arora *et al.*, 2000). In this study, myriocin decreased membrane fluidity (Fig. 3A), which is consistent with the decrease in membrane fluidity observed in silymarin-treated cells in another study (Yun and Lee, 2017).

Phospholipids are the main components of eukaryotic cell membranes and consist of glycerophospholipids and sphingolipids. In glycerophospholipid metabolism, the main metabolites are glycerophospholipids, including PC (Morii *et al.*, 2014), PE (Kimblehill *et al.*, 2018), PG (Patiño-Márquez *et al.*, 2018) and PI (Collin and Cochet, 2013). The hypothetical protein *FOXG_06093* (XP_018241738.1), which is involved in the synthesis of PE, *FOXG_03186* and its encoded protein (methylene-fatty-acyl-phospholipid synthase), which are involved in the synthesis of PC, phosphatidylserine (XP_018244080.1), which is involved in the synthesis of CDP-diacylglycerol synthase, and *FOXG_10104*, *FOXG_04329* and phosphatidylserine synthase (XP_018246094.1), which are involved in the synthesis of PG, were all significantly downregulated at the mRNA and protein levels in myriocin-treated cells. Moreover, phospholipase D (XP_018240842.1), which is involved in the synthesis of 1,2-dimyristoyl-sn-glycero-3-phosphatidylcholine (DMPC), and CDP-diacylglycerol-inositol 3-phosphatidyltransferase (XP_018243765.1), which is involved in the synthesis of PI, were significantly upregulated in myriocin-treated cells. Myriocin significantly reduced the expression levels of genes and proteins and affected the content of phospholipids, which thereby led to the damage to cell membrane and ultimately inhibited the growth of *Fon*. Methylene-fatty-acyl-phospholipid synthase was a key enzyme in the synthesis of PC and played an important role in the protein interaction network (Fig. 6). The decrease in the expression of methylene-fatty-acyl-phospholipid synthase might have led to the decrease in the expression of multiple proteins and change the content of multiple phospholipids. Moreover, the contents of PC and DMPC on the surface of the lipid membrane were changed; this may cause damage to the cell membrane (Nabika *et al.*, 2016). In a study, changes in the content of PI have been reported to result in the decreased fluidity of the membrane (Andoh *et al.*, 2016). In this study, the decrease of membrane fluidity in myriocin-treated cells might be due to the influence of myriocin on PI content.

Sphingolipid metabolism has been known to play a role in cell death, survival and therapy resistance (Beckham *et al.*, 2013). *De novo* sphingolipid metabolism is initiated by serine palmitoyl transferase (SPT) (Perry, 2002). In this study, myriocin induced the overexpression of *FOXG_11535* and SPT, or it directly interacted with

SPT (Fig. 8) and then caused the overexpression of *FOXG_11535*. The overexpression of *FOXG_11535* (Fig. 6A) led to the upregulation of other genes in the pathway, and then, SPT interacted with other proteins (Fig. 6), which may cause the overexpression of proteins in the entire pathway. Finally, sphingolipid metabolism was upregulated in myriocin-treated cells. Organisms are exposed to life-threatening risks that may disrupt sphingolipid metabolism. The upregulation of sphingolipid metabolism may be related to the resistance of *Fon* to myriocin treatment (Tani and Funato, 2018). L-Serine and palmitoyl-CoA are catalysed by SPT, which reacts with other enzymes to synthesize excess dihydrosphingosine and dihydroceramide. These reactions may cause a decrease in membrane fluidity (Andoh *et al.*, 2016) and result in the damage to the *Fon* cell membrane and eventually cell death (Suh *et al.*, 2018). In this study, SPT exhibited higher activities at MIC ($1.25 \mu\text{g ml}^{-1}$) and 2MIC ($2.50 \mu\text{g ml}^{-1}$) than at 4MIC ($5.0 \mu\text{g ml}^{-1}$) and 8MIC ($10 \mu\text{g ml}^{-1}$) (Fig. 8B). This might be due to the resistance of *Fon* to myriocin treatment (MIC, $1.25 \mu\text{g ml}^{-1}$ and 2MIC, $2.50 \mu\text{g ml}^{-1}$) by increasing SPT activity. The inhibition of SPT activities at 4MIC ($5.0 \mu\text{g ml}^{-1}$) and 8MIC ($10 \mu\text{g ml}^{-1}$) might reduce the total level of sphingolipids in cells and cause a strong growth defect (Tani and Funato, 2018). Furthermore, myriocin affected SPT activity as evidenced through molecular docking (Fig. 8).

Nascent membrane proteins are located adjacent to ER membrane proteins throughout their integration and translation (Thrift *et al.*, 1991). In this study, the expression levels of genes and proteins in protein processing in the endoplasmic reticulum pathway were decreased; this might lead to defects in ER membrane and membrane proteins. In a study, the protein transporter *sec-13* (XP_018241549.1) was reported to be involved in the formation of double-membrane transport vesicles from the ER to the Golgi (Bouain *et al.*, 2014). Moreover, the expression levels of the protein transporter *sec-13* were significantly downregulated when *Fon* was exposed to myriocin, which could block the synthesis of transport vesicles and ultimately prevent membrane proteins from reaching the cell membrane (Kaneko *et al.*, 2019). In addition, the E3 ubiquitin-protein ligase synoviolin (XP_018238877.1), which reduce the ubiquitination of target proteins and retard the cells growth (You *et al.*, 2016), was significantly downregulated in myriocin-treated cells.

ATP-binding cassette (ABC) transporters constitute a superfamily of membrane proteins that are responsible for the translocation of many molecules across membranes with ATP (Rees *et al.*, 2009). In this study, the expression levels of some genes and proteins related to ABC transporters were altered or disrupted by myriocin. For example, the *FOXG_20796* gene and protein

(XP_018251339.1), which are related to the translocation of iron-sulfur clusters, were significantly downregulated in myriocin-treated cells; this effect may cause abnormal metabolism and membrane damage (Do *et al.*, 2018). Moreover, *FOXG_15633* was upregulated by myriocin; this upregulation might be related to the resistance of *Fon* to myriocin (Dolberg and Reichl, 2017) and indicate the adjustment of *Fon* growth to myriocin.

Steroid biosynthesis is a classic target of antifungal compounds (Song *et al.*, 2019b). In the steroid biosynthesis pathway, the main metabolites are sterols, including cholesterol, lanosterol, sitosterol, sterol and ergosterol (Fujita *et al.*, 2018). Ergosterol plays an important role in membrane-bound enzyme activity, membrane fluidity, membrane integrity and substrate transport (Ferrante *et al.*, 2016). In this study, the expression levels of *FOXG_01590* and C-8 sterol isomerase (XP_018234407.1), which are related to the synthesis of ergosterol, were upregulated in myriocin-treated cells (Fig. 6). Furthermore, methylsterol monooxygenase (XP_018244831.1) and hypothetical protein *FOXG_09168* (XP_018246232.1) were significantly downregulated in myriocin-treated cells. Also, the expression of *FOXG_04703* and methylsterol monooxygenase (XP_018244831.1) was significantly downregulated, which would thereby reduce steroid biosynthesis, destroy the cell membrane structure, change membrane-bound enzyme activity, decrease membrane fluidity and cause damage to the *Fon* cell membrane (Scheinflug *et al.*, 2017). These results suggest that some membrane-related genes and proteins are targets for myriocin action.

Conclusion

The mechanisms of myriocin on the *Fon* cell membrane are shown in Figure 9. Myriocin decreased cell membrane fluidity, destroyed membrane integrity, induced leakage of calcein, caused shrinkage of cell morphology and inhibited *Fon* growth or induced cell death. The damage to the cell membrane of *Fon* was caused by the altered or disrupted expression of some membrane-related genes and proteins at the mRNA and protein levels; these genes and proteins mainly include those related to sphingolipid metabolism, glycerophospholipid metabolism, steroid biosynthesis, ABC transporters and protein processing in the endoplasmic reticulum. In conclusion, myriocin exhibited potent antifungal effects on *Fon* via membrane disruption.

Experimental procedures

Experimental preparation

The *Fon* used in this study was provided by the Laboratory of Microbial Ecology, Qiqihar University in China (Xu

et al., 2019). *Fon* mycelium was incubated in potato dextrose agar (PDA) Petri dishes in the dark at 28°C for 5 days to induce sporulation. The dishes were soaked in sterile distilled water, and the conidia were separated from the culture surface with a brush. Afterwards, sterile four-layer cheesecloth was used for the filtration of the suspension and removal of mycelial fragments. A hemocytometer was used to establish a conidia concentration of 1.0×10^6 CFU (colony-forming units) ml^{-1} . Myriocin and amphotericin B were dissolved in DMSO and diluted into final concentrations (MIC, $1.25 \mu\text{g ml}^{-1}$; 2MIC, $2.5 \mu\text{g ml}^{-1}$; 4MIC, $5 \mu\text{g ml}^{-1}$ and 8MIC, $10 \mu\text{g ml}^{-1}$; amphotericin B, $1.25 \mu\text{g ml}^{-1}$) with DMSO at concentrations less than or equal to 1% (Wadsworth *et al.*, 2013).

Observation of conidial morphologies by scanning and transmission electron microscopy

To observe the morphological changes of conidia caused by myriocin, electron microscopy was used. The *Fon* conidial suspensions were incubated with myriocin for 12 h at final concentrations of MIC ($1.25 \mu\text{g ml}^{-1}$), 2MIC ($2.50 \mu\text{g ml}^{-1}$), 4MIC ($5.0 \mu\text{g ml}^{-1}$) and 8MIC ($10 \mu\text{g ml}^{-1}$). For scanning electron microscopy (SEM), the myriocin-treated conidia were centrifuged at 8000 r.p.m. for 5 min and prefixed with 2.5% glutaraldehyde. The fixed cells were washed three times for 10 min with 100 mM phosphate buffer, post-fixed for 3 h in 1% osmium tetroxide and dehydrated through a series of ethanol gradient solutions. The samples were then coated with gold and observed on a scanning electron microscope (S-3400, Hitachi, Japan). For transmission electron microscopy (TEM) observation, the samples were embedded in Epon 812, sectioned using an ultramicrotome and imaged under a transmission electron microscope (H-7650, Hitachi, Japan). The negative control (CK1) consisted of *Fon* conidial suspensions mixed without myriocin, and the positive control (CK2) consisted of conidial suspensions mixed with amphotericin B at a final concentration of $1.25 \mu\text{g ml}^{-1}$. The experiment was repeated three times, and each treatment consisted of three replicates.

Analysis of *Fon* membrane integrity

According to the methods described by Sun *et al.* (2015), the effect of myriocin on *Fon* membrane integrity was analysed by using LIVE/DEAD BacLight™ Viability Kit (MA, USA) under confocal laser scanning microscopy (CLSM). SYTO 9 stains both live and dead cells, whereas propidium iodide (PI) permeates cells only when the membrane is broken, reducing the SYTO 9 fluorescence when both dyes are present. Thus, cells with intact membranes are stained by SYTO 9 and emit green fluorescence, whereas the cells with damaged

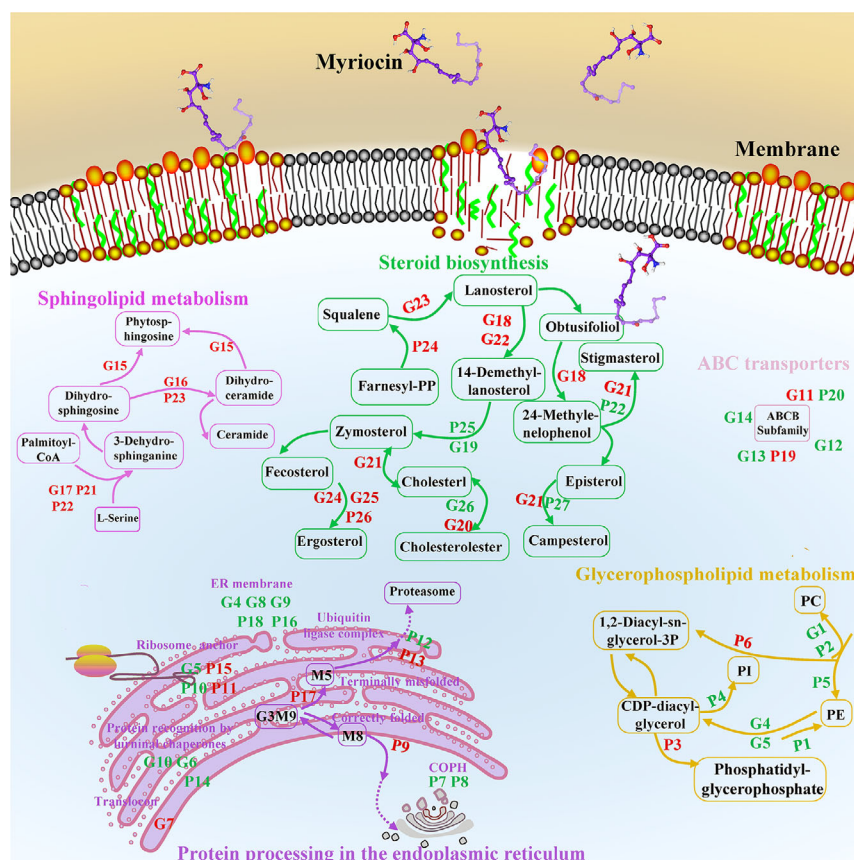


Fig. 9. Schematic diagram of the mechanism of myriocin on the *Fon* cell membrane. Myriocin damaged *Fon* cell membrane. The damage to the cell membrane of *Fon* was caused by the altered or disrupted expression of some membrane-related genes and proteins at the mRNA and protein levels; these genes and proteins mainly including those related to sphingolipid metabolism, glycerophospholipid metabolism, steroid biosynthesis, ABC transporters and protein processing in the endoplasmic reticulum. The red and green letters represent upregulated and downregulated of genes and proteins, respectively. The DEGs and DEPs are listed in Table S6.

membranes are stained by PI and emit red fluorescence (Liu *et al.*, 2017). The *Fon* conidial suspensions were mixed with myriocin at final concentrations of MIC ($1.25 \mu\text{g ml}^{-1}$), 2MIC ($2.50 \mu\text{g ml}^{-1}$), 4MIC ($5.0 \mu\text{g ml}^{-1}$) and 8MIC ($10 \mu\text{g ml}^{-1}$), and the mixtures were incubated for 12 h. The mixtures incubated for 12 h without myriocin was considered the negative control (CK1), and the mixtures with amphotericin B (final concentrations: $1.25 \mu\text{g ml}^{-1}$) was considered the positive control (CK2). The incubated conidial suspensions were centrifuged at 8000 r.p.m. for 5 min at 4°C . Then, the conidia were resuspended in phosphate-buffered saline (PBS). Subsequently, $1.5 \mu\text{l}$ of SYTO 9 and $1.5 \mu\text{l}$ of PI were added, and the mixture was incubated for 30 min at $25 \pm 2^\circ\text{C}$ in the dark. Afterwards, the mixtures were centrifuged. The localization of fluorescent dye in the conidia was visualized by using a confocal laser scanning microscope (TCS SP8, Leica, Germany) at $63\times$ and excitation wavelengths of 488 nm (green conidia) and 535 nm (red conidia).

Determination of cell membrane fluidity

The fluorescence polarization (P) and anisotropy (r) were determined by using 1,6-diphenyl-1,3,5-hexatriene (DPH) (Wang *et al.*, 2019). The *Fon* conidial suspensions were incubated for 12 h with myriocin at final concentrations of MIC ($1.25 \mu\text{g ml}^{-1}$), 2MIC ($2.50 \mu\text{g ml}^{-1}$), 4MIC ($5.0 \mu\text{g ml}^{-1}$) and 8MIC ($10 \mu\text{g ml}^{-1}$). The mixtures incubated for 12 h without myriocin was considered the control (CK1). Afterwards, the mixtures were centrifuged at 8000 r.p.m. for 5 min, washed three times and resuspended in PBS. Then, $5 \mu\text{l}$ of $100 \mu\text{mol l}^{-1}$ DPH solution was mixed with 10 ml of the conidial suspension. After incubation at 30°C for 30 min, fluorescence polarization and anisotropy were measured at excitation/emission wavelengths $\lambda_{\text{ex}}/\lambda_{\text{em}} = 360 \text{ nm}/427 \text{ nm}$ by using a fluorescence spectrophotometer (F-7000, Hitachi, Japan) equipped with a polarizer.

Preparation of calcein-loaded liposomes and leakage assay

Phosphatidylcholine (PC), phosphatidylethanolamine (PE), phosphatidylinositol (PI) and ergosterol were purchased from Sigma-Aldrich, Shanghai, China. One type of liposome was prepared as follows: PC/PE/PI/ergosterol with a mass ratio of 5:4:1:2 to mimic the fungal cell membrane was mixed (Sun *et al.*, 2015). Calcein-loaded liposomes were prepared according to methods described by Lee & Lee, (2015). Phospholipids were dissolved in chloroform and methanol at a ratio of 5:4:1:2. After vacuum evaporation and drying overnight, 1.5 ml of dye buffer (70 mM calcein, 10 mM Tris, 150 mM NaCl, and 0.1 mM EDTA, pH 7.4) was added to the dried sample. Then, the mixture was freeze-thawed in liquid nitrogen until homogeneous and passed through 0.22- μm polycarbonate filters. The uncoated calcein was removed by gel filtration through a Sephadex G-50 column and elution with phosphate buffer. The calcein-loaded liposomes were diluted to 90 mM for further testing. For the calcein leakage assay, a suspension of liposomes containing calcein was treated with myriocin at final concentrations of MIC ($1.25 \mu\text{g ml}^{-1}$), 2MIC ($2.50 \mu\text{g ml}^{-1}$), 4MIC ($5.0 \mu\text{g ml}^{-1}$) and 8MIC ($10 \mu\text{g ml}^{-1}$). The sample without myriocin was considered the control (CK1). The leakage of calcein from liposomes was measured by using a fluorescence spectrophotometer (F-7000, Hitachi, Japan) at an excitation wavelength of 485 nm and an emission wavelength of 515 nm. Then, 20 μl of 10% Triton X-100 (pH 7.4) was added into the mixture at 12 min to determine the maximum fluorescence intensity of 100% calcein leakage. The percentage of calcein leakage induced by myriocin was calculated according to the equation calcein leakage (%) = $100 \times (F - F_0) / (F_T - F_0)$, where F represents the fluorescence intensity acquired after the addition of myriocin, and F_0 and F_T represent the fluorescence intensities without myriocin and with Triton X-100 respectively (Bakonyi *et al.*, 2018). The statistical data are presented as mean \pm standard deviation of three replicates.

Illumina library and RNA-Seq

According to the returned results, treatment including myriocin at MIC and 8MIC were selected for further study, and $0 \mu\text{g ml}^{-1}$ myriocin was considered the control (CK1). Three biological replicates were prepared for the treatment groups and the control. *Fon* conidia were exposed to various myriocin concentrations for 12 h; the mixtures were centrifuged at 8000 r.p.m. for 10 min and then frozen in liquid nitrogen immediately for RNA extraction and RNA sequencing (RNA-Seq).

The total RNA was extracted from the samples by using TRIzol[®] Reagent according the manufacturer's instructions (Invitrogen, USA) and was treated with DNase I (TaKara, Kofu, Japan) to remove genomic the DNA. Then, the quality and concentration of the RNA were determined by using a 2100 Bioanalyzer (Agilent, Palo Alto, CA, USA) and a NanoDrop spectrophotometer (ND-2000, Thermo, USA). Afterwards, high-quality total RNA samples ($\text{OD}_{260/230} \geq 2.0$, $\text{OD}_{260/280} = 1.8\text{--}2.2$, $\text{RIN} \geq 6.5$, $18\text{S} : 18\text{S} \geq 1.0$, $> 2 \mu\text{g}$) were used to construct the sequencing libraries.

The RNA-Seq library was prepared following the Tru-Seq[™] RNA sample preparation kit from Illumina (San Diego, CA). First-strand cDNA was synthesized by using random hexamer primers, and double-stranded cDNA was subsequently synthesized by using a SuperScript Double-Strand cDNA Synthesis kit (Invitrogen, Carlsbad, CA, USA). PCR amplification was performed by using Phusion DNA polymerase (NEB) for 15 PCR cycles. The PCR amplification products were quantified by using TBS380 (PicoGreen), and the pair-end RNA sequencing library was sequenced by using the Illumina HiSeq 4000 platform with 2×150 bp reads.

The raw paired-end reads were trimmed and controlled for quality by using SeqPrep (<https://github.com/jstjohn/SeqPrep>) and Sickle (<https://github.com/najoshi/sickle>). Then, the clean reads were separately aligned to the reference genome with orientation mode by using TopHat software, and the mapped results were then queried by using BLAST against the database (<ftp://ftp.ncbi.nlm.nih.gov/blast/executables/blast+/2.9.0/>). The FPKM method was used to compare the differences in gene expression among samples. The software package EdgeR was used to determine the fold change of transcripts and to screen differentially expressed genes (DEGs) (Song *et al.*, 2019a). The criteria of significant differential expression were fold change ≥ 2 or ≤ 0.5 and adjusted P -value ≤ 0.05 (Jian *et al.*, 2017). Gene Ontology (GO) and the Kyoto Encyclopedia of Genes and Genomes (KEGG) were used for annotation (Wang *et al.*, 2016).

Protein extraction and LC-MS/MS analysis

Treatment with myriocin at MIC ($1.25 \mu\text{g ml}^{-1}$) or 8MIC ($10 \mu\text{g ml}^{-1}$) was used for the proteomics study, and $0 \mu\text{g ml}^{-1}$ myriocin was considered the control (CK1). *Fon* conidia were exposed to various myriocin concentrations for 12 h; the mixtures were centrifuged at 8000 r.p.m. for 10 min and then frozen in liquid nitrogen immediately for label-free quantitative proteomic analysis. Each treatment was performed in triplicate for proteomic analysis. The proteins from samples were extracted by using an extraction buffer (1% SDS,

200 mM dithiothreitol, 50 mM Tris-HCl and 1% protease inhibitor, pH 8.8). Then, the samples were centrifuged at 12 000 r.p.m. at 4°C for 20 min, and the supernatants were precipitated with precooled acetone at -20°C overnight. Afterwards, the precipitate was collected and washed twice with 90% precooled acetone. Then, the protein precipitate was redissolved in lysis buffer (8 M urea, 1% SDS and 1% protease inhibitor). The lysates were centrifuged, and the protein concentration of the supernatant was quantified by using the bicinchoninic acid (BCA) method. Protein digestion was performed according to standard procedure previously reported (Morris *et al.*, 2019). Briefly, the appropriate amount of trichloroethyl phosphate was added to each sample tube containing 150 µg of protein and incubated at 37°C for 60 min. The protein sample was resuspended in 150 µl of buffer (100 mM TEAB). Trypsin was added to approximately 150 µg of protein for each sample at an enzyme: protein ratio of 1:50 and digested at 37°C overnight. The peptides were desalted with OASIS[®] HLB µElution plates and vacuum dried. Peptide concentrations were determined by using a peptide quantification kit (Thermo, Cat. 23275). LC-MS/MS analysis was performed on a Q Exactive[™] mass spectrometer (MS) (1200-6430A, Agilent, USA) (Zhong *et al.*, 2018). The peptides were loaded onto a C18-reverse phase column (75 µm × 25 cm, Thermo, USA) with buffer A (2% acetonitrile and 0.1% formic acid) and separated with a linear gradient of buffer B (80% acetonitrile and 0.1% formic acid) at a flow rate of 300 µL/min. Afterwards, the peptides were subjected to nanoelectrospray ionization followed by tandem MS in Q Exactive (Thermo, USA). Intact peptides were detected in the orbitrap at a resolution of 70 000. Peptides were selected for MS/MS using a high-energy collisional dissociation (HCD) setting of 20. Ion fragments were identified in the orbitrap at a resolution of 17 500.

Proteomics data processing

MS/MS spectra were searched using ProteomeDiscover[™] Software 2.2 against the *Fusarium oxysporum* database (27347s, 20190328). Trypsin digestion was selected with cleavage specificity allowing up to two missing cleavages. Carbamidomethyl on cysteine was assigned as a fixed modification, and oxidation on methionine and protein N-terminal acetylation were specified as variable modifications. Differentially expressed proteins (DEPs) between the two samples were screened with fold change > 1.2 or < 0.83 and *P*-value < 0.05. The analysis of membrane-related DEPs was performed, including protein functional annotation, GO functional annotation and KEGG pathway enrichment analysis.

The correlation of DEG-DEG or DEP-DEP was revealed by using cluster heat maps and network interactions, and the relationship between DEGs and their corresponding DEPs was explored.

RT-qPCR

To verify the RNA-Seq results, 9 DEGs from the RNA-Seq analysis were selected, and RT-qPCR was performed to confirm the expression changes of these 9 DEGs. RT-qPCR was performed on the RNA samples used for RNA-seq. Total cellular RNA was quantified at OD₂₆₀ and OD₂₈₀ by using a SMA400 microspectrophotometer (Merinton, Beijing, China). The single-stranded cDNA of total RNA was generated by using RevertAid Premium Reverse Transcriptase (EP0733, Thermo Scientific, MA, USA), and the cDNA samples were stored at -20°C for later use (Hu *et al.*, 2019a). Quantitative real-time PCR was performed on a StepOne Plus Real-Time PCR instrument (ABI, Waltham, MA, USA). The primers used for RT-qPCR are listed in Table S1, and the *18S rRNA* gene was used as the internal control to which normalization of the mRNA abundance between samples was performed. Each qRT-PCR reaction system (20 µl) included 10 µl of 2 × SYBR Green qPCR Master Mix, 0.4 µl of forward primer (10 µM), 0.4 µl of reverse primer (10 µM), 2 µl of template (cDNA) and 7.2 µl of ddH₂O. PCR was performed as follows: 3 min at 95°C, 45 cycles of 5 s at 95°C and 30 s at 60°C. A melting curve was generated to detect the specificity of the amplification. A relative quantitative analysis was calculated by using the 2^{-ΔΔCt} method. Each measurement was performed in triplicate.

Assay of SPT activity and molecular docking

The myriocin and conidia solution were mixed at different concentrations (MIC, 1.25 µg ml⁻¹; 2MIC, 2.50 µg ml⁻¹; 4MIC, 5.0 µg ml⁻¹; and 8MIC, 10 µg ml⁻¹; CK1, 0 µg ml⁻¹). After 12-h incubation, the mixtures were centrifuged at 8000 r.p.m. for 10 min, washed three times and resuspended in PBS. The conidia were cryo-crushed by using an ultrasonic cell disrupter (JY-92IIDN, Scientz, China) according to the following procedure: 45 cycles of 3-s ultrasonic time and 3-s interval time. Then, the supernatants were centrifuged at 8000 r.p.m. for 10 min and transferred onto 96-microwell plates. The SPT in the supernatant was extracted by using an enzyme-linked immunosorbent assay kit (ELISA, Blobase, Zhangqiu, China) according to the manufacturer's protocol, and the activity of SPT was measured by using a microplate reader (PT-3502, Potenov, Tongzhou, China) (Hu *et al.*, 2019b). Each treatment was performed in triplicates.

Homology modelling is a computational procedure that aims to build a three-dimensional (3D) protein model (for unknown crystallographic structures) by using known structures of homologous protein as templates. In this study, we used SWISS-MODEL to derive the 3D structure of SPT (XP_018249811.1) from SPT amino acid sequences (query sequence). The amino acid sequence of the SPT in this study was acquired through NCBI and automatically compared. The template of the homology modelling was from the SPT crystal structure (PDB ID: 4bmk.1.A) in the Protein Data Bank (PDB). The homology model was constructed through the SWISS-MODEL (<http://swissmodel.expasy.org>) server (Waterhouse *et al.*, 2018).

For molecular docking, the 3D structure of myriocin was downloaded from the PubChem (<https://pubchem.ncbi.nlm.nih.gov/>) website. The molecular docking of myriocin (ligand) to the 3D protein model of SPT (XP_018249811.1) was performed by using UCSF DOCK 6 (Xie and Minh, 2019). Both the protein (SPT) and ligand (myriocin) molecules were prepared prior to docking analysis by using the Prepare Protein and Prepare Ligand steps, respectively. The generation of the 3D conformation of myriocin was attained by using the Prepare Ligands tool, and the 3D conformation of myriocin with the lowest grid score was considered the 'best docking model'. Afterwards, protein–ligand (myriocin) interactions were analysed. A diagram of the docking model was made by using the FREE MAESTRO module in Schrodinger 2018 Software and MS PowerPoint (PPT) 2013. The docking process was performed by using the default parameters.

Statistical analysis

SPSS 26.0 software was used for the statistical analysis of the data. The data are expressed as mean \pm standard error from three biological replicates. The *t*-test was used for statistical analysis; $P \leq 0.05$ was considered significant.

Acknowledgements

The authors gratefully acknowledge the funding of this work by the National Natural Science Foundation of China (31700428), the Joint Guiding Project of Natural Science Foundation in Heilongjiang Province, China (LH2019C068), the Open Foundation of Key Laboratory of Urban Agriculture, the Ministry of Agriculture and Rural Areas, China (UA201904), and the Scientific Research Program at Qiqihar University, China (135209266).

Conflict of interest

None declared.

References

- Andoh, Y., Aoki, N., and Okazaki, S. (2016) Molecular dynamics study of lipid bilayers modeling the plasma membranes of mouse hepatocytes and hepatomas. *J Chem Phys* **144**: 85104.
- Arora, A., Byrem, T.M., Nair, M.G., and Strasburg, G.M. (2000) Modulation of liposomal membrane fluidity by flavonoids and isoflavonoids. *Arch Biochem Biophys* **373**: 102–109.
- Bakonyi, M., Gacsi, A., Berko, S., Kovacs, A., and Csanyi, E. (2018) Stratum corneum lipid liposomes for investigating skin penetration enhancer effects. *RSC Adv* **8**: 27464–27469.
- Beckham, T.H., Cheng, J.C., Marrison, S.T., Norris, J.S., and Liu, X. (2013) Interdiction of sphingolipid metabolism to improve standard cancer therapies. *Adv Cancer Res* **117**: 1–36.
- Bouain, N., Shahzad, Z., Rouached, A., Khan, G.A., Berthomieu, P., Abdelly, C., *et al.* (2014) Phosphate and zinc transport and signalling in plants: toward a better understanding of their homeostasis interaction. *J Exp Bot* **65**: 5725–5741.
- Cao, Y., Pi, H.L., Chandrangsu, P., Li, Y.T., Wang, Y.Q., Zhou, H., *et al.* (2018) Antagonism of two plant-growth promoting *Bacillus velezensis* isolates against *Ralstonia solanacearum* and *Fusarium oxysporum*. *Sci Rep-UK* **8**: 4360.
- Cavanagh, R.J., Smith, P.A., and Stolnik, S. (2019) Exposure to a nonionic surfactant induces a response akin to heat-shock apoptosis in intestinal epithelial cells: implications for excipients safety. *Mol Pharm* **16**: 618–631.
- Chen, Y., Wang, J., Yang, N., Wen, Z., Sun, X., Chai, Y., and Ma, Z. (2018) Wheat microbiome bacteria can reduce virulence of a plant pathogenic fungus by altering histone acetylation. *Nat Commun* **9**: 3429.
- Cho, J., Choi, H., Lee, J., Kim, M.S., Sohn, H.Y., and Lee, D.G. (2013) The antifungal activity and membrane-disruptive action of dioscin extracted from *Dioscorea nipponica*. *BBA-Biomembranes* **1828**: 1153–1158.
- Collin, S., and Cochet, F. (2013) Phosphatidylinositol synthase activity from plant membrane fractions and from *E. coli*-expressed recombinant peptides. *Method Mol Biol* **1009**: 145–161.
- Costa, A.E.S., Cunha, F.S.D., Honorato, A.D.C., Capucho, A.S., Dias, R.D.C.S., Borel, J.C., and Ishikawa, F.H. (2018) Resistance to *Fusarium* Wilt in watermelon accessions inoculated by chlamydozoospores. *Sci Hortic* **228**: 181–186.
- Cronjé, T.F., and Gaynor, P.T. (2019) Electroporation of Ishikawa cells: analysis by flow cytometry. *IET Nanobiotechnol* **13**: 58–65.
- De Melo, N.R., Abdrahman, A., Greig, C., Mukherjee, K., Thornton, C.A., Ratcliffe, N.A., *et al.* (2013) Myriocin significantly increases the mortality of a non-mammalian model host during candida pathogenesis. *PLoS One* **8**: e78905.
- Do, E., Park, S., Li, M., Wang, J., Ding, C., Kronstad, J.W., and Jung, W.H. (2018) The mitochondrial ABC transporter Atm1 plays a role in iron metabolism and virulence in the human fungal pathogen *Cryptococcus neoformans*. *Med Mycol* **56**: 458–468.

- Dolberg, A.M., and Reichl, S. (2017) Activity of multidrug resistance-associated proteins 1–5 (MRP1–5) in the RPMI 2650 cell line and explants of human nasal turbinates. *Mol Pharm* **14**: 1577–1590.
- Dou, J., Zhao, S., Lu, X., He, N., and Liu, W. (2018) Genetic mapping reveals a candidate gene (CIFS1) for fruit shape in watermelon (*Citrullus lanatus* L.). *Theor Appl Genet* **131**: 947–958.
- Everts, K.L., Egel, D.S., Langston, D., and Zhou, X.G. (2014) Chemical management of *Fusarium* wilt of watermelon. *Crop Prot* **66**: 114–119.
- Falardeau, J., Wise, C., Novitsky, L., and Avis, T.J. (2013) Ecological and mechanistic insights into the direct and indirect antimicrobial properties of *Bacillus subtilis* lipopeptides on plant pathogens. *J Chem Ecol* **39**: 869–878.
- Ferrante, T., Barge, A., Taramino, S., Oliaro-Bosso, S., and Balliano, G. (2016) 4-Methylzymosterone and other intermediates of sterol biosynthesis from yeast mutants engineered in the ERG27 gene encoding 3-Ketosteroid reductase. *Lipids* **51**: 1103–1113.
- Fujita, S., Hasegawa, T., Nishiyama, Y., Fujisawa, S., Nakano, Y., Nada, T., *et al.* (2018) Interaction between orexin A and bone morphogenetic protein system on progesterone biosynthesis by rat granulosa cells. *J Steroid Biochem* **181**: 73–79.
- Gumbo, J.R., Cloete, T.E., Van Zyl, G.J.J., and Somerville, J.E.M. (2014) The viability assessment of *Microcystis aeruginosa* cells after co-culturing with *Bacillus mycoides* B16 using flow cytometry. *Phys Chem Chem Phys* **72**: 24–33.
- Hu, Y., Zhang, X., Cui, M., Wang, M., Su, Z., Liao, Q., and Zhao, Y. (2019a) Circular RNA profile of parathyroid neoplasms: analysis of co-expression networks of circular RNAs and mRNAs. *RNA Biol* **16**: 1228–1236.
- Hu, D., Zhang, D., Liu, B., Zhou, Y., Yu, Y., Shen, L., *et al.* (2019b) Optimization of preparation of rat kidney decellularized scaffold by combining freeze-thawing with perfusion. *Chin J Chem* **35**: 307–318.
- Jian, W., Faisal, I., Lan, L., Meijuan, L., Chong, Y., Xiaoli, J., *et al.* (2017) Complementary RNA-Sequencing based transcriptomics and iTRAQ proteomics reveal the mechanism of the alleviation of quinclorac stress by salicylic acid in *Oryza sativa* ssp. *japonica*. *Int J Mol Sci* **18**: 1975.
- Jiang, C.H., Wu, F., Yu, Z.Y., Xie, P., and Guo, J.H. (2015) Study on screening and antagonistic mechanisms of *Bacillus amyloliquefaciens* 54 against bacterial fruit blotch (BFB) caused by *Acidovorax avenae* subsp. *citulli*. *Microbiol Res* **170**: 95–104.
- Jiang, C.H., Yao, X.F., Mi, D.D., Li, Z.J., Yang, B.Y., Zheng, Y., *et al.* (2019) Comparative transcriptome analysis reveals the biocontrol mechanism of *Bacillus velezensis* F21 against *Fusarium* wilt on watermelon. *Front Microbiol* **10**: 652.
- Kaneko, T., Minohara, T., Shima, S., Yoshida, K., Fukuda, A., Iwamori, N., *et al.* (2019) A membrane protein, TMCO5A, has a close relationship with manchette microtubules in rat spermatids during spermiogenesis. *Mol Reprod Dev* **86**: 330–341.
- Kimblehill, A.C., Petrache, H.I., Seifert, S., and Firestone, M.A. (2018) Reorganization of ternary lipid mixtures of nonphosphorylated phosphatidylinositol interacting with angiominin. *J Phys Chem B* **122**: 8404–8415.
- Koumoutsis, A., Chen, X.H., Henne, A., Liesegang, H., Hitzeroth, G., Franke, P., *et al.* (2004) Structural and functional characterization of gene clusters directing nonribosomal synthesis of bioactive cyclic lipopeptides in *Bacillus amyloliquefaciens* strain FZB42. *J bacteriol* **186**: 1084–1096.
- Lee, W., and Lee, D.G. (2015) Fungicidal mechanisms of the antimicrobial peptide Bac8c. *BBA-Biomembranes* **1848**: 673–679.
- Li, L., Shi, Y., Cheng, X., Xia, S., Cheserek, M.J., and Le, G. (2015) A cell-penetrating peptide analogue, P7, exerts antimicrobial activity against *Escherichia coli* ATCC25922 via penetrating cell membrane and targeting intracellular DNA. *Food Chem* **166**: 231–239.
- Li, Y., Xiang, Q., Zhang, Q., Huang, Y., and Su, Z. (2012) Overview on the recent study of antimicrobial peptides: Origins, functions, relative mechanisms and application. *Peptides* **37**: 207–215.
- Liu, G., Ren, G., Zhao, L., Cheng, L., Wang, C., and Sun, B. (2017) Antibacterial activity and mechanism of bifidocin a against *Listeria monocytogenes*. *Food Control* **73**: 854–861.
- Massart, S., Perazzolli, M., Höfte, M., Pertot, I., and Jijakli, M. (2015) Impact of the omic technologies for understanding the modes of action of biological control agents against plant pathogens. *Biocontrol* **60**: 725–746.
- Molinatto, G., Puopolo, G., Sonogo, P., Moretto, M., Engelen, K., Viti, C., *et al.* (2016) Complete genome sequence of *Bacillus amyloliquefaciens* subsp. *plantarum* S499, a rhizobacterium that triggers plant defences and inhibits fungal phytopathogens. *J Biotechnol* **238**: 56–59.
- Morii, H., Ogawa, M., Fukuda, K., and Taniguchi, H. (2014) Ubiquitous distribution of phosphatidylinositol phosphate synthase and archaetidylinositol phosphate synthase in Bacteria and Archaea, which contain inositol phospholipid. *Biochem Biophys Res Commun* **443**: 86–90.
- Morrin, S.T., Owens, R.A., LeBerre, M., Gerlach, J.Q., Joshi, L., Bode, L., *et al.* (2019) Interrogation of milk-driven changes to the proteome of intestinal epithelial cells by integrated proteomics and glycomics. *J Agr Food Chem* **67**: 1902–1917.
- Nabika, H., Sakamoto, A., Motegi, T., Tero, R., Yamaguchi, D., and Unoura, K. (2016) Imaging characterization of cluster-induced morphological changes of a model cell membrane. *J Phys Chem C* **120**: 15640–15647.
- Ongena, M., and Jacques, P. (2008) *Bacillus* lipopeptides: versatile weapons for plant disease biocontrol. *Trends Microbiol* **16**: 115–125.
- Patel, H., Tscheka, C., Edwards, K., Karlsson, G., and Heerklotz, H. (2011) All-or-none membrane permeabilization by fengycin-type lipopeptides from *Bacillus subtilis* QST713. *Biochim Biophys Acta* **1808**: 2000–2008.
- Patiño-Márquez, I.A., Manrique-Moreno, M., Patiño-González, E., Jemiola-Rzemińska, M., and Strzalka, K. (2018) Effect of antimicrobial peptides from *Galleria mellonella* on molecular models of *Leishmania* membrane. Thermotropic and fluorescence anisotropy study. *J Antibiot* **71**: 642–652.

- Perry, D.K. (2002) Serine palmitoyltransferase: Role in apoptotic de novo ceramide synthesis and other stress responses. *BBA-Mol Cell Biol Lipid* **1585**: 146–152.
- Rees, D.C., Johnson, E., and Lewinson, O. (2009) ABC transporters: the power to change. *Nat Rev Mol Cell Bio* **10**: 218–227.
- Scheinpflug, K., Krylova, O., and Strahl, H. (2017) Measurement of cell membrane fluidity by laurdan GP: Fluorescence spectroscopy and microscopy. *Antibiotics* **1520**: 159–174.
- Song, J., Shang, N., Baig, N., Yao, J., Shin, C., Kim, B.K., et al. (2019b) *Aspergillus flavus* squalene synthase as an antifungal target: Expression, activity, and inhibition. *Biochem Biophys Res Commun* **512**: 517–523.
- Song, X., Zhong, L., Lyu, N., Liu, F., Li, B., Hao, Y., et al. (2019a) Inulin can alleviate metabolism disorders in ob/ob mice by partially restoring leptin-related pathways mediated by gut microbiota. *Genom Proteom Bioinform* **17**: 64–75.
- Spampinato, C., and Leonardi, D. (2013) Candida infections, causes, targets, and resistance mechanisms: traditional and alternative antifungal agents. *Biomed Res Int* **2013**:1–13.
- Spyr, C.A., Käsermann, F., and Kempf, C. (1995) Identification of the pore forming element of *Semliki Forest* virus spikes. *FEBS Lett* **375**: 134–136.
- Suh, J.H., Degagne, E., Gleghorn, E.E., Setty, M., Rodriguez, A., Park, K.T., et al. (2018) Sphingosine-1-Phosphate signaling and metabolism gene signature in pediatric inflammatory bowel disease: a matched-case control pilot study. *Inflamm Bowel Dis* **24**: 1321–1334.
- Sun, Y., Dong, W., Sun, L., Ma, L., and Shang, D. (2015) Insights into the membrane interaction mechanism and antibacterial properties of chensinin-1b. *Biomaterials* **37**: 299–311.
- Tani, M., and Funato, K. (2018) Protection mechanisms against aberrant metabolism of sphingolipids in budding yeast. *Curr Genet* **64**: 1021–1028.
- Thimon, L., Peypoux, F., Wallach, J., and Michel, G. (1995) Effect of the lipopeptide antibiotic, iturin A, on morphology and membrane ultrastructure of yeast cells. *FEMS Microbiol Lett* **128**: 101–106.
- Thomsen, R., and Christensen, M.H. (2006) MolDock: a new technique for high-accuracy molecular docking. *J Med Chem* **49**: 3315–3321.
- Thrift, R.N., Andrews, D.W., Walter, P., and Johnson, A.E. (1991) A nascent membrane protein is located adjacent to ER membrane proteins throughout its integration and translation. *J Cell Biol* **112**: 809–821.
- Wadsworth, J.M., Clarke, D.J., McMahon, S.A., Lowther, J., Beattie, A.E., Langridgesmith, P.R.R., et al. (2013) The chemical basis of serine palmitoyltransferase inhibition by myriocin. *J Am Chem Soc* **135**: 14276–14285.
- Wan, T., Zhao, H., and Wei, W. (2018) Effects of the biocontrol agent *Bacillus amyloliquefaciens* SN16-1 on the rhizosphere bacterial community and growth of tomato. *J Phytopathol* **166**: 324–332.
- Wang, J., Lv, M., Islam, F., Gill, R.A., Yang, C., Ali, B., et al. (2016) Salicylic acid mediates antioxidant defense system and ABA pathway related gene expression in *Oryza sativa* against quinclorac toxicity. *Ecotoxicol Environ Safe* **133**: 146–156.
- Wang, Z.G., Zhu, X.H., Su, Y.P., Xu, W.H., Liu, H., Liu, Z.P., et al. (2019) Dimethyl phthalate damaged the cell membrane of *Escherichia coli* K12. *Ecotoxicol Environ Safe* **180**: 208–214.
- Waterhouse, A., Bertoni, M., Bienert, S., Studer, G., Tauriello, G., Gumienny, R., et al. (2018) SWISS-MODEL: homology modelling of protein structures and complexes. *Nucleic Acids Res* **46**: W296–W303.
- Wu, Y.C., Zhou, J.Y., Li, C.G., and Ma, Y. (2019) Antifungal and plant growth promotion activity of volatile organic compounds produced by *Bacillus amyloliquefaciens*. *MicrobiologyOpen* **8**: e00813.
- Xie, B., and Minh, D. D. L. (2019) Alchemical grid dock (AlGDock) calculations in the D3R grand challenge 3: Binding free energies between flexible ligands and rigid receptors. *J Computer Aid Mol Des* **33**: 61–69.
- Xu, Z., Shao, J., Li, B., Yan, X., Shen, Q., and Zhang, R. (2013) Contribution of bacillomycin D in *Bacillus amyloliquefaciens* SQR9 to antifungal activity and biofilm formation. *Appl Environ Microb* **79**: 808–815.
- Xu, W., Wang, H., Lv, Z., Shi, Y., and Wang, Z. (2019) Antifungal activity and functional components of cell-free supernatant from *Bacillus amyloliquefaciens* LZN01 inhibit *Fusarium oxysporum* f. sp. *niveum* growth. *Biotechnol Biotech Equipment* **33**: 1042–1052.
- Yamaji-Hasegawa, A., Takahashi, A., Tetsuka, Y., Senoh, Y., and Kobayashi, T. (2005) Fungal metabolite sulfamisterin suppresses sphingolipid synthesis through inhibition of serine palmitoyltransferase. *Biochemistry* **44**: 268–277.
- Yan, X., Liang, X., Jin, S., Lv, J., and Wang, D. (2010) Primary study on mode of action for macrocyclic fungicide candidates (7B3, D1) against *rhizoctonia solani kuhn*. *J Agric Food Chem* **58**: 2726–2729.
- You, Q., Zhai, K., Yang, D., Yang, W., Wu, J., Liu, J., et al. (2016) An E3 ubiquitin ligase-BAG protein module controls plant innate immunity and broad-spectrum disease resistance. *Cell Host Microbe* **20**: 758–769.
- Yun, D.G., and Lee, D.G. (2017) Silymarin exerts antifungal effects via membrane-targeted mode of action by increasing permeability and inducing oxidative stress. *BBA-Mol Basis Dis* **1859**: 467–474.
- Zhang, B., Dong, C., Shang, Q., Han, Y., and Li, P. (2013) New insights into membrane-active action in plasma membrane of fungal hyphae by the lipopeptide antibiotic bacillomycin L. *BBA-Mol Basis Dis* **1828**: 2230–2237.
- Zhang, X., Wang, Y., Liu, L., Wei, Y., and Li, P. (2016) Two-peptide bacteriocin PlnEF causes cell membrane damage to *Lactobacillus plantarum*. *Biochem Biophys Acta* **1858**: 274–280.
- Zhao, Y.J., Selvaraj, J.N., Xing, F.G., Zhou, L., Wang, Y., Song, H.M., et al. (2014) Antagonistic action of *Bacillus subtilis* strain SG6 on *Fusarium graminearum*. *PLoS One* **9**: e92486.
- Zhong, Y., Chen, B., Li, J., Yang, Q.J., and Cai, C. (2018) Analysis of fatty acids and metabolites in plasma by LC-MS/MS. *J Chin Chem Soc-Taipei* **39**: 310–315.

Supporting information

Additional supporting information may be found online in the Supporting Information section at the end of the article.

Fig. S1. The proportions of differentially coloured of conidia treated with myriocin. MIC, $1.25 \mu\text{g ml}^{-1}$ myriocin; 2MIC, $2.5 \mu\text{g ml}^{-1}$ myriocin; 4MIC, $5 \mu\text{g ml}^{-1}$ myriocin; 8MIC, $10 \mu\text{g ml}^{-1}$ myriocin; CK1, $0 \mu\text{g ml}^{-1}$ myriocin as negative control; CK2, $1.25 \mu\text{g ml}^{-1}$ amphotericin B as positive control.

Table S1. Genes and primers used in RT-qPCR validation.

Table S2. The information and pathway names of 27 DEPs.

Table S3. The information and pathway names of 26 DEGs.

Table S4. The KEGG pathway category and ID and name of pathway.

Table S5. DEGs and its corresponding DEPs.

Table S6. Names and spots of 26 DEGs and NCBI accessions and spots of 27 DEPs.